Nonlinear equilibrium of partially liquid-filled tanks: A finite element/level-set method to handle hydrostatic follower forces

Christophe Hoareau, Jean-François Deü

Nonlinear equilibrium of partially liquid-filled tanks: a finite element/level-set method to handle hydrostatic follower forces

C. Hoareau, J.-F. Deü

Laboratoire de Mécanique des Structures et des Systèmes Couplés (LMSSC)
Conservatoire national des arts et métiers (Cnam)

292 Rue Saint-Martin, 75003 Paris, France

Abstract

This paper deals with the nonlinear finite element computation of the pre-stressed state of structures partially filled with an incompressible inviscid liquid. The fluid is modeled by hydrostatic follower forces such that no volumetric fluid mesh is needed. Large deformations are taken into account and lead to the fluid height variation of the wetted surface to satisfy the fluid volume conservation. The main originality of this work lies on the use of a level-set approach to handle numerical integration on the fluid-structure interface. The method is developed on 3D problems considering a finite element quadratic mesh. Various numerical examples are computed using a Newton-Raphson algorithm and a quadratic convergence rate is reached by using consistent tangent stiffness operators.

Keywords: Hydrostatic follower forces, Finite element, Finite deformation, Volume conservation, Level-set method, Quadratic mesh

☆Fully documented templates are available in the elsarticle package on CTAN.

*Corresponding author

E-mail address: christophe.hoareau@lecnam.net (Laboratoire de Mécanique des Structures et des Systèmes Couplés (LMSSC)
Conservatoire national des arts et métiers (Cnam)).

URL: http://www.lmssc.cnam.fr/ (Laboratoire de Mécanique des Structures et des Systèmes Couplés (LMSSC)
Conservatoire national des arts et métiers (Cnam))

2010 MSC: 00-01, 99-00

1. Introduction

This paper deals with the finite element computation of the nonlinear equilibrium of elastic structures partially filled with liquid. The objective is to evaluate the prestressed state of flexible tanks in finite deformation. Those computational results could be useful to estimate the influence of geometrical nonlinearties on the linearized vibrations of such coupled systems, inducing for example a shift of the hydroelatsic natural circular frequencies [1, 2, 3]. In this study, since the liquid is supposed inviscid, incompressible and at rest, without considering surface tension effects, its mechanical action on the structure is assumed to be an hydrostatic follower force. The major contribution of the paper lies on the use of the level-set approach [4] for the numerical integration of finite element operators used in the nonlinear solution algorithm (e.g. the external nodal forces and the load stiffness matrix [5]).

The literature on the computation of finite deformation of elastic structures partially filled with liquid and gas, through a finite element approach, have been already treated in [6] for volume-dependent pressure, in [7] for hydrostatic dependent pressure and in [8] for gas and fluid supported membrane. The stability of thin-walled shell is examined in [9] and the influence of modifications of the shape of multi-chamber systems filled with gas and liquid is analysed in [10]. The key points of all these approaches are the computation of the displacement-dependent external forces and the symmetric load stiffness matrix used inside an increment of the nonlinear algorithms (e.g. Newton-Raphson or arc-length continuation approaches). Due to the incompressibility assumption, the pressure can be expressed as a function of structural displacement at the wetted interface and consequently, no volumetric fluid mesh is needed. This kind of ap-

proaches have been used in recent years for the analysis of unstable hyperelastic membranes [11], possibly with non-uniform thickness [12], and for parametric and multiparametric stability analyses [13, 14]. The nonlinear equilibrium of flexible floating structures subjected to external hydrostatic pressure is also presented in [15]. Finally, note that a large collection of shell and plate theories, containing many examples with follower forces, has been published recently in [16].

The level-set approach, which constitutes the main originality of the paper, is used to handle the numerical integration on current loaded surface elements, which are no more coincident with the contact line. In the case of linear partially wetted surface elements, a particular numerical treatment based on cutted elements has been proposed in [11, 15]. Here, since the structure is meshed with an hexahedral quadratic mesh, we propose an original implementation of the level-set, on height nodes curved quadratic surface elements, which necessitates the development of multiples cases exposed in the paper. This method allows the user to obtain (i) an accurate position of Gauss points for the numerical integration and (ii) a curvilinear mesh discretization of the current contact line.

The outline of the paper is the following. In Section 2, we recall the nonlinear finite element equations of a structure submitted to hydrostatic follower forces, considering an hyperelastic constitutive law. A variational formulation based on the classic three-dimensional Lagrangian approach is presented and a finite element discretization is performed using a quadratic hexaedral mesh. In Section 3, we detail the operators obtained by linearization of the virtual external work for a Newton-Raphson algorithm. Then, Section 4 presents the definition of a continuation method based on arc-length constraint to pass through instabilities. In Section 5, we explain how to evaluate the wetted surface by a level-set approach. Finally, in Section 6, numerical applications are analyzed to show the effectiveness of the proposed approach.

2. Nonlinear finite element equations

2.1. Problem description

We consider a fluid-structure interaction problem in which the fluid is supposed to be inviscid, incompressible, irrotational, without surface tension and at rest. The fluid loading on the structure corresponds to a hydrostatic pressure $p(z,t)$ supported by the solid external normal $\mathbf{n}$ at the current fluid-structure interface, also called the wetted surface Σ. The hydrostatic pressure field is defined by (see Fig. 1)

$$\begin{aligned} p(\mathbf{x},t) &= 0 && \text{if} \quad z \geqslant h \\ p(\mathbf{x},t) &= -\rho g(z-h) && \text{if} \quad z < h \end{aligned} \tag{1}$$

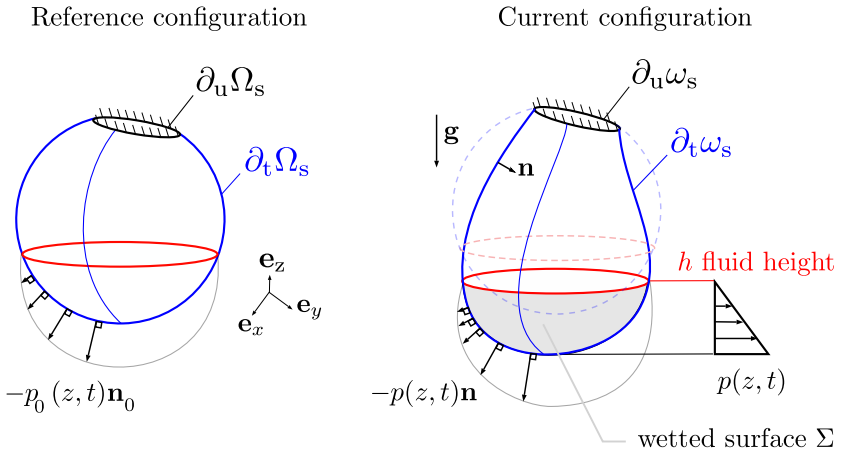

Figure 1: Structure in its reference configuration Ω_{s} and its current configuration ω_{s} loaded by hydrostatic follower forces (only the internal face of the tank with the follower forces are presented).

where ρ is the fluid density, h the free-surface height and $\mathbf{x} = x\mathbf{e}_x + y\mathbf{e}_y + z\mathbf{e}_z$ the coordinate vector field in the current configuration at time t. Also, we note $\mathbf{X}$ the coordinate vector in the reference configuration and $\mathbf{F} = \frac{\partial \mathbf{x}}{\partial \mathbf{X}}$ the deformation gradient. A constraint must be taken into account in the model:

the internal fluid volume contained below the free-surface eight is constant due to the incompressibility assumption.

2.2. Solid hypotheses and constitutive relations

We consider an isotropic, homogeneous, elastic and nearly-incompressible material for the structure such as rubber or organic tissue subject to large deformation, so the use of a hyperelastic constitutive law is relevant. This law implies the existence of a strain-energy Ψ per unit volume [17]. A classical approach is to separate this potential Ψ in two parts [18]: the volumetric potential Ψ_{vol} and the isochoric potential Ψ_{iso}. Thus, it is convenient to introduce the modified Cauchy-Green tensor $\overline{\mathbf{C}} = J^{\frac{2}{3}}\mathbf{C}$ where $J = \det(\mathbf{F})$ and $\mathbf{C} = \mathbf{F}^{\mathrm{T}}\mathbf{F}$ such that the potential is defined by

$$\Psi = \Psi_{\text{vol}}(J) + \Psi_{\text{iso}}\left(\overline{C}_I, \overline{C}_{II}\right) \tag{2}$$

where $\overline{C}_I = C_I C_{III}^{-\frac{1}{3}}$, $\overline{C}_{II} = C_{II} C_{III}^{-\frac{2}{3}}$ are the first two modified invariant of $\overline{\mathbf{C}}$ with $C_I = \mathrm{tr}(\mathrm{C})$, $C_{II} = \frac{1}{2}[\mathrm{tr}^2(\mathrm{C}) - \mathrm{tr}(\mathrm{C}^2)]$ and $C_{III} = \det(\mathrm{C})$. For the isochoric potential, we consider a Mooney-Rivlin model described by

$$\Psi_{\text{iso}} = c_{10}\left(\overline{C}_I - 3\right) + c_{01}\left(\overline{C}_{II} - 3\right) \tag{3}$$

where c_{10} and c_{01} are material coefficients obtained by fitting experimental data. Note that $c_{01} = 0$ corresponds to a Neo-Hookean model. Then, the volumetric potential energy is given by

$$\Psi_{\text{vol}} = \frac{k_0}{2}(J-1)^2 \tag{4}$$

where k_0 is the bulk modulus. Multiple derivations of Ψ lead to the second Piola-Kirchhoff tensor and the fourth-order elasticity tensor such that

$$\mathbf{S} = 2\frac{\partial \Psi}{\partial \mathbf{C}} \quad \text{and} \quad \mathbb{D} = 4\frac{\partial^2 \Psi}{\partial \mathbf{C}^2} \tag{5}$$

To express all operators, which depend on the hyperelastic potentials, we invite the reader to refer to [19, 20]. In those references, operators are given for various constitutive laws relating the Green-Lagrange strain tensor $\mathbf{E} = \frac{1}{2}(\mathbf{C} - \mathbf{I})$ and the second Piola-Kirchhoff stress tensor $\mathbf{S}$.

2.3. Nonlinear equations and discretized problem

Local equations in the current configuration ω_s and on its boundary $\partial\omega_s$ are obtained under the hypotheses described previously, and in particular without volumic forces, as

$$\mathrm{div}\boldsymbol{\sigma} = \mathbf{0} \qquad \text{in} \quad \omega_s \tag{6}$$

$$\boldsymbol{\sigma}\,\mathbf{n} = -p(\mathbf{x},t)\,\mathbf{n} \qquad \text{on} \quad \partial_t\omega_s \tag{7}$$

$$\mathbf{u} = \mathbf{0} \qquad \text{on} \quad \partial_u\omega_s \tag{8}$$

where $\boldsymbol{\sigma}$ is the Cauchy stress tensor. From Eqs. (6), (7) and (8), the weak formulation in the current configuration is given by

$$\int_{\omega_s} \boldsymbol{\sigma} : \delta\boldsymbol{\epsilon}\, dv = -\int_{\partial_t\omega_s} \delta\mathbf{u}\cdot p(\mathbf{x},t)\,\mathbf{n}\, ds, \quad \forall\, \delta\mathbf{u} \in \mathcal{C}_u \tag{9}$$

where $\delta\boldsymbol{\epsilon} = \frac{1}{2}(\mathbf{grad}\,\delta\mathbf{u} + \mathbf{grad}^T\delta\mathbf{u})$ is the virtual eulerian strain tensor (symmetric part of the virtual displacement gradient with respect to the current configuration, i.e. $\mathbf{grad}\,\bullet = \frac{\partial \bullet}{\partial \mathbf{x}}$ and $\mathcal{C}_u$ is the kinematic admissible space of smooth enough functions. This formulation is written in the reference configuration Ω_s and on its boundary $\partial\Omega_s$ by

$$\int_{\Omega_s} \mathbf{S} : \delta\mathbf{E}\, dV = -\int_{\partial_t\Omega_s} \delta\mathbf{u}\cdot p_0(\mathbf{x},t)\mathbf{n}_0\, dS, \quad \forall\, \mathbf{u} \in \mathcal{C}_u \tag{10}$$

where $\delta\mathbf{E} = \frac{1}{2}(\delta\mathbf{F}^T\,\mathbf{F} + \mathbf{F}^T\,\delta\mathbf{F})$ is the virtual Green-Lagrange strain tensor with $\delta\mathbf{F} = \mathbf{Grad}\,\delta\mathbf{u}$ and $\mathbf{Grad}\,\bullet = \frac{\partial \bullet}{\partial \mathbf{X}}$. For the discretization of the structure, we consider 3D finite elements with quadratic shape functions (e.g. hexaedric 20 nodes elements as seen in Fig. 2). For details about the nonlinear finite-element procedures and numerical implementation, the readers can refer to [21, 22]. Considering a three-dimensional discretization, all the nonlinear terms of the 3D potential energy are taken into account in the model. We shall recall that other approaches exist in which shell and plate theories have been developed [16], possibly taking into account the thickness of thick shell structures [23]

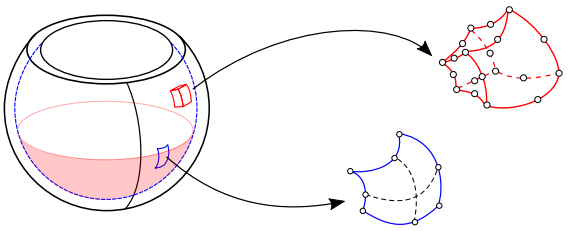

Figure 2: FE discretization

The finite element discretization of this classical weak formulation on the reference configuration leads to the nonlinear equilibrium equation

$$\mathbf{F}_{\text{int}}(\mathbf{q}) - \mathbf{F}_{\text{ext}}(\mathbf{q}) = \mathbf{0} \tag{11}$$

where $\mathbf{F}_{\text{ext}}$ and $\mathbf{F}_{\text{int}}$ are respectively the external and internal nodal forces.

2.4. Tangent stiffness matrices

A classical resolution method based on a Newton-Raphson algorithm is used in this paper. At each iterations, we have to solve a linear system

$$\mathbf{K}_{\text{tan}}\Delta\mathbf{q} = \mathbf{R} \tag{12}$$

where $\mathbf{R} = \mathbf{F}_{\text{ext}} - \mathbf{F}_{\text{int}}$ is the out of balance vector and $\mathbf{K}_{\text{tan}}$ is the tangent stiffness matrix given by

$$\mathbf{K}_{\text{tan}} = \mathbf{K}_{\text{mat}} + \mathbf{K}_{\text{geo}} - \mathbf{K}_{\text{fol}} \tag{13}$$

with $\mathbf{K}_{\text{mat}}$ the material tangent stiffness matrix [17, 19], $\mathbf{K}_{\text{geo}}$ the geometrical tangent stiffness matrix [24] and $\mathbf{K}_{\text{fol}}$ the follower tangent stiffness matrix [5, 7, 25]. In the following, only $\mathbf{K}_{\text{fol}}$ is detailed since the other terms are widely explained in the literature.

2.5. Nodal hydrostatic external forces

To express $\mathbf{F}_{\text{ext}}$, we consider the discretized virtual external work associated with the right hand side of Eq. (9) and the hydrostatic pressure field given by Eq. (1) such that

$$\delta W^{\text{h}}_{\text{ext}} = -\int_{\Sigma^h} \delta\mathbf{u}^{\text{h}} \cdot p\,\mathbf{n}\,ds \tag{14}$$

$$= \rho g \int_{\Sigma^h_0} \delta\mathbf{u}^{\text{h}} \cdot \left(z^{\text{h}} - h\right) \left(\mathbf{x}^{\text{h}}_{,\xi} \times \mathbf{x}^{\text{h}}_{,\eta}\right) dS \tag{15}$$

$$= \delta\mathbf{q}^{\text{T}}\mathbf{F}_{\text{ext}} \tag{16}$$

where the indice $\bullet^{\text{h}}$ is associated to a finite element discretization, Σ^{h} is the discretized wetted surface in the current configuration, Σ^h_0 is defined by two parameters (ξ, η), dS is the reference surface element such that $dS = d\xi d\eta$ and $\delta\mathbf{q}$ is the nodal virtual displacement vector. As seen in Eq. (15), the follower forces depend on the current configuration coordinates $\mathbf{x}$ and the fluid height h.

3. Linearization of the virtual external work

3.1. Linearized virtual external work

In a continuous framework, the linearization of the virtual external energy is written as

$$\Delta\delta W_{\text{ext}} = -\int_{\Sigma} \delta\mathbf{u} \cdot \left(\Delta p\,\mathbf{n} + p\,\Delta\mathbf{n}\right) ds \tag{17}$$

where Δp and $\Delta\mathbf{n}$ are respectively the pressure and the normal variations related to a small displacement variation $\Delta\mathbf{u}$. According to Eq. (1), the expression of the hydrostatic pressure variation is given by

$$\Delta p = -\rho_{\text{f}} g(\Delta z - \Delta h) \tag{18}$$

where Δh is the variation of the fluid height to respect the incompressibility of the fluid. We can thus rewrite Eq. (17) as follow

$$\Delta\delta W_{\text{ext}} = \underbrace{-\int_\Sigma \delta\mathbf{u}\cdot p\,\Delta\mathbf{n}\,ds + \rho_{\text{f}} g\int_\Sigma \delta\mathbf{u}\cdot\Delta z\,\mathbf{n}\,ds}_{\Delta\delta W_\Sigma(\Delta\mathbf{u},\delta\mathbf{u})} \underbrace{-\rho_{\text{f}} g\int_\Sigma \delta\mathbf{u}\cdot\Delta h\,\mathbf{n}\,ds}_{\Delta\delta W_V(\Delta\mathbf{u},\delta\mathbf{u})} \tag{19}$$

where the form $\Delta\delta W_\Sigma$ is due to the normal variation and the displacement of the wetted surface on the pressure field contributions, and $\Delta\delta W_V$ is due to the fluid height elevation contribution coming from the fluid volume conservation. As explained below, those two bilinear forms are symmetric.

3.2. Symmetry of the bilinear forms

Symmetry of $\Delta\delta W_\Sigma$: A proof of the symmetry of $\Delta\delta W_\Sigma$ has been given in [5] for constant pressure, in [1, 7, 8, 9] for hydrostatic pressure using surface operators and in [26] using volumetric ones. Let us precise that, inside each increment, due to the following identity:

$$\Delta\delta W_\Sigma(\Delta\mathbf{u},\delta\mathbf{u}) - \Delta\delta W_\Sigma(\delta\mathbf{u},\Delta\mathbf{u}) = -\oint_{\partial\Sigma} p\,(\delta\mathbf{u}\times\Delta\mathbf{u})\cdot\mathbf{dl} \tag{20}$$

the Eq. (20) is null when (i) $p = 0$ on $\partial\Sigma$ or (ii) $\delta\mathbf{u} = \mathbf{0}$ on $\partial\Sigma$, where $\partial\Sigma$ is the boundary of the wetted surface. Even if other cases can exist (see e.g. [7]), all the examples presented in Section 6 satisfies a combination of those two conditions.

Symmetry of $\Delta\delta W_V$: The proof of the symmetry of $\Delta\delta W_V$ is based on geometric considerations due to the fluid volume conservation during a Newton-Raphson iteration [1, 7] (illustrated by Fig. 3). The relation between Δh and $\Delta\mathbf{u}$ is given by

$$\Delta h = \frac{1}{|\,A_{\text{f}}\,|}\int_\Sigma \Delta\mathbf{u}\cdot\mathbf{n}\,ds \quad \text{with} \quad A_{\text{f}} = \int_\Sigma \mathbf{n}\cdot\mathbf{e}_z\,ds \tag{21}$$

The expression of $\Delta\delta W_V$ is thus given by

$$\Delta\delta W_V(\Delta\mathbf{u},\delta\mathbf{u}) = -\frac{\rho_{\text{f}} g}{|\,A_{\text{f}}\,|}\int_\Sigma \delta\mathbf{u}\cdot\mathbf{n}\,ds\int_\Sigma \Delta\mathbf{u}\cdot\mathbf{n}\,ds \tag{22}$$

where the symmetry is directly proven due to the following relation

$$\Delta\delta W_V(\Delta\mathbf{u}, \delta\mathbf{u}) = \Delta\delta W_V(\delta\mathbf{u}, \Delta\mathbf{u}) \tag{23}$$

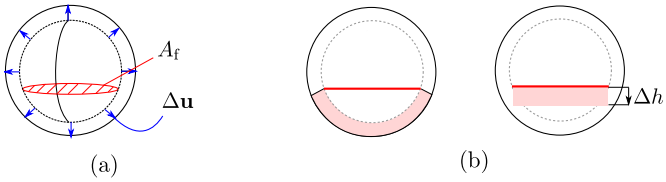

Figure 3: (a) Linearized displacement (blue arrows) of the internal face between a given configuration (dashed line) to the next configuration (black line) and the initial free surface area (red hatched surface); (b) In the sectional view, the red volume generated by the linearized displacement through the wetted surface is supposed equal to the red volume generated by the free surface base cylinder of height Δh.

3.3. Discretized tangent stiffness matrices

The tangent stiffness matrices are detailed in this sub-section. Firstly, we briefly recall the calculus of the symmetric part of $\Delta\delta W_\Sigma$. Let's focus on the two terms of the $\Delta\delta W_\Sigma$ form

$$\Delta\delta W_\Sigma(\Delta\mathbf{u}, \delta\mathbf{u}) = \underbrace{-\int_\Sigma \delta\mathbf{u}\cdot p\,\Delta\mathbf{n}\,ds}_{\Delta\delta W_\Sigma^{(\mathrm{a})}} + \underbrace{\rho_\mathrm{f} g\int_\Sigma \delta\mathbf{u}\cdot\Delta z\,\mathbf{n}\,ds}_{\Delta\delta W_\Sigma^{(\mathrm{b})}} \tag{24}$$

In practice, the computation of the tangent stiffness matrix depends on the surface parametrization such that

$$\Delta\delta W_\Sigma^{(\mathrm{a})} = -\int_{\Sigma_0}\delta\mathbf{u}\cdot p\,(\Delta\mathbf{u}_{,\xi}\times\mathbf{x}_{,\eta} + \mathbf{x}_\xi\times\Delta\mathbf{u}_{,\eta})\,dS \tag{25}$$

$$\Delta\delta W_\Sigma^{(\mathrm{b})} = \rho_\mathrm{f} g\int_{\Sigma_0}\delta\mathbf{u}\cdot(\Delta\mathbf{u}\cdot\mathbf{e}_z)(\mathbf{x}_{,\xi}\times\mathbf{x}_{,\eta})\,dS \tag{26}$$

Due to the proofs recalled previously, we only keep the symmetric parts of Eqs. (25) and (26) in the following. After integration by parts and some mathematical

manipulations, we obtain

$$\begin{aligned}\Delta\delta W_\Sigma = \quad & \frac{1}{2}\int_{\Sigma_0} p\,[\delta\mathbf{u}\cdot\,(\mathbf{x}_{,\eta}\times\Delta\mathbf{u}_{,\xi}) - \delta\mathbf{u}_{,\xi}\cdot\,(\mathbf{x}_{,\eta}\times\Delta\mathbf{u})]\,dS \\ & + \frac{1}{2}\int_{\Sigma_0} p\,[\delta\mathbf{u}_{,\eta}\cdot(\mathbf{x}_{,\xi}\times\Delta\mathbf{u}) - \delta\mathbf{u}\cdot\,(\mathbf{x}_{,\xi}\times\Delta\mathbf{u}_{,\eta})]\,dS \\ & + \frac{\rho_\mathrm{f} g}{2}\int_{\Sigma_0}[(\Delta\mathbf{u}\cdot\mathbf{e}_z)\delta\mathbf{u} + (\delta\mathbf{u}\cdot\mathbf{e}_z)\Delta\mathbf{u}]\cdot(\mathbf{x}_{,\xi}\times\mathbf{x}_{,\eta})\,dS \end{aligned} \tag{27}$$

Then, by considering Eq. (27), the discretized form of $\Delta\delta W_\Sigma$ is given by

$$\begin{aligned}\Delta\delta W_\Sigma(\Delta\mathbf{u}^\mathrm{h},\delta\mathbf{u}^\mathrm{h}) = \quad & \delta\mathbf{q}^\mathrm{T}\frac{1}{2}\int_{\Sigma_0^\mathrm{h}} p\,(\mathbf{N}^\mathrm{T}\boldsymbol{\Omega}_\eta\mathbf{N}_{,\xi} - \mathbf{N}_{,\xi}^\mathrm{T}\boldsymbol{\Omega}_\eta\mathbf{N})\,dS\,\Delta\mathbf{q} \\ & + \delta\mathbf{q}^\mathrm{T}\frac{1}{2}\int_{\Sigma_0^\mathrm{h}} p\,(\mathbf{N}_{,\eta}^\mathrm{T}\boldsymbol{\Omega}_\xi\mathbf{N} - \mathbf{N}^\mathrm{T}\boldsymbol{\Omega}_\xi\mathbf{N}_{,\eta})\,dS\,\Delta\mathbf{q} \\ & + \delta\mathbf{q}^\mathrm{T}\frac{\rho_\mathrm{f} g}{2}\int_{\Sigma_0^\mathrm{h}} \mathbf{N}^\mathrm{T}((\mathbf{x}_{,\xi}^\mathrm{h}\times\mathbf{x}_{,\eta}^\mathrm{h})\mathbf{e}_\mathrm{z}^\mathrm{T} + \mathbf{e}_\mathrm{z}(\mathbf{x}_{,\xi}^\mathrm{h}\times\mathbf{x}_{,\eta}^\mathrm{h})^\mathrm{T})\mathbf{N}dS\,\Delta\mathbf{q} \\ & = \delta\mathbf{q}^\mathrm{T}\,\mathbf{K}_\Sigma\,\Delta\mathbf{q} \end{aligned} \tag{28}$$

where $\mathbf{K}_\Sigma$ is the tangent stiffness matrix due to the contribution of the normal variation and the small Δz variation of the wetted surface, $\boldsymbol{\Omega}_\xi$ and $\boldsymbol{\Omega}_\eta$ are the screw matrices respectively associated to the cross product of the derivatives of the coordinate vectors $\mathbf{x}_{,\xi}^\mathrm{h}$ and $\mathbf{x}_{,\eta}^\mathrm{h}$.

Then, according to Eq. (22), the discretized form of $\Delta\delta W_V$ can be directly written as

$$\begin{aligned}\Delta\delta W_V(\Delta\mathbf{u}^\mathrm{h},\delta\mathbf{u}^\mathrm{h}) = & -\delta\mathbf{q}^\mathrm{T}\,\rho_\mathrm{f} h\int_{\Sigma_0^\mathrm{h}}\mathbf{N}^\mathrm{T}(\mathbf{x}_{,\xi}^\mathrm{h}\times\mathbf{x}_{,\eta}^\mathrm{h})dS\int_{\Sigma_0^\mathrm{h}}(\mathbf{x}_{,\xi}^\mathrm{h}\times\mathbf{x}_{,\eta}^\mathrm{h})^\mathrm{T}\mathbf{N}\,dS\,\Delta\mathbf{q} \\ & = \delta\mathbf{q}\,\mathbf{K}_V\Delta\mathbf{q} \end{aligned} \tag{29}$$

where $\mathbf{K}_V$ is the tangent stiffness due to the fluid height variation contribution.

Finally, the tangent stiffness matrix $\mathbf{K}_\mathrm{fol}$ is the sum of $\mathbf{K}_\Sigma$ and $\mathbf{K}_V$.

In this section, we detailed the discretized follower tangent stiffness matrix $\mathbf{K}_\mathrm{fol}$, when the loading is parameterized by the fluid height h for clamped structures ($\mathbf{u}_\mathrm{u} = \mathbf{0}$ on $\partial_\mathrm{d}\omega$). The same operators can be used for the computation of the equilibrium of partially filled tanks, without fluid volumetric mesh, in the following cases:

- for non-zero prescribed displacement ($\mathbf{u}_\mathrm{d} \neq \mathbf{0}$ on $\partial_\mathrm{u}\omega$);
- for a given prescribed amount of fluid volume V_f;
- for unstable problems (e.g. buckling or wrinkling issues).

Those three cases are formulated in Section 4 to give some details about the numerical implementation, and analyzed in Section 6 through numerical examples .

4. Specific aspects of the numerical resolution method

4.1. Prescribed displacement with Lagrange multiplier

The numerical examples on Section 6 are subjected to a prescribed displacement such that

$$\mathbf{u} = \mathbf{u}_\mathrm{d} \quad \text{on} \quad \partial_\mathrm{u}\Omega_\mathrm{s} \tag{30}$$

We briefly describe here our approach to handle prescribed displacement with Lagrange multiplier. The discretized problem is given by

$$\begin{cases} \mathbf{F}_\mathrm{int}(\mathbf{q}) - \mathbf{F}_\mathrm{ext}(\mathbf{q}) + \mathbf{B}^\mathrm{T}\boldsymbol{\lambda} &= \mathbf{0} \\ \mathbf{B}\mathbf{q} &= \mathbf{q}_\mathrm{d} \end{cases} \tag{31}$$

where $\boldsymbol{\lambda}$ are the unknown Lagrange multipliers of the problem and $\mathbf{B}$ is a rectangular matrix satisfying the Dirichlet boundary conditions. The linearized problem consists in solving the following linear system

$$\begin{bmatrix} \mathbf{K}_\mathrm{tan} & \mathbf{B}^\mathrm{T} \\ \mathbf{B} & \mathbf{O} \end{bmatrix} \begin{pmatrix} \Delta\mathbf{q} \\ \Delta\boldsymbol{\lambda} \end{pmatrix} = \begin{pmatrix} \mathbf{F}_\mathrm{ext}(\mathbf{q}) - \mathbf{F}_\mathrm{int}(\mathbf{q}) - \mathbf{B}\boldsymbol{\lambda} \\ \mathbf{q}_\mathrm{d} - \mathbf{B}\mathbf{q} \end{pmatrix} \tag{32}$$

The residual criterion used to stop our Newton-Raphson algorithm is given by the $\mathcal{L}_2$-norm of the out of balance vector which is the right hand side of Eq. (32). In Section 6, this method is used either to compute the pres-stretched states of elastic membranes with large deformations or to impose large rotation of a partially filled tank with a fluid volume constraint.

4.2. Fluid volume computation without volumetric mesh

If the fluid volume V_f have to be constant during a simulation, the fluid height is reevaluated by using a bisection method at each Newton-Raphson iteration. We consider in Fig. 4 a fluid domain Ω_f bounded by the wetted surface Σ and the free surface Γ, under the assumption of an horizontal free-surface (because no surface tension is taken into account in this study). Considering an appropriate

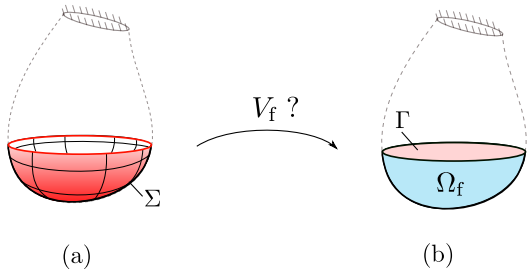

Figure 4: (a) The wetted surface Σ used for the computation of the fluid volume V_f; (b) Volumetric fluid domain Ω_f and its plane free-surface Γ.

vector field $\mathbf{Z}$ such that $\mathrm{div}(\mathbf{Z}) = 1$ (e.g. $\mathbf{Z} = (z-h)\mathbf{e}_z$), the internal fluid volume is given by

$$V_\mathrm{f} = \int_{\Omega_\mathrm{f}} dV \tag{33}$$

$$= \int_{\Omega_\mathrm{f}} \mathrm{div}\left[(z-h)\mathbf{e}_z\right] dV \tag{34}$$

$$= \int_{\Sigma} (z-h)\mathbf{e}_z \cdot \mathbf{n}\, ds + \int_{\Gamma} (z-h)\mathbf{e}_z \cdot \mathbf{n}\, ds \tag{35}$$

The term on the free surface vanish because the free surface is horizontal (i.e. $z = h$), so we obtain

$$V_\mathrm{f} = \int_{\Sigma} (z-h)\mathbf{e}_z \cdot \mathbf{n}\, ds \tag{36}$$

The previous equation is then used to check the fluid volume at each N-R iteration to evaluate the fluid height with a bisection method. This will be used in some examples of Section 6 to satisfy the incompressibility condition of the fluid by only using the wetted surface mesh.

4.3. Arc-length continuation method

Taking into account geometrical nonlinearities and follower forces may lead to instabilities as buckling or wrinkling [6, 13]. A classical Newton-Raphson algorithm is no longer appropriate to find the quasi-static equilibrium state, so a continuation method have been implemented to pass through the instabilities. One possibility is to define the nonlinear equilibrium such that λ is an unknown parameter controlling the fluid level

$$\mathbf{G}\left(\mathbf{q},\lambda\right)=\mathbf{F}_{\text{int}}\left(\mathbf{q}\right)-\mathbf{F}_{\text{ext}}\left(\mathbf{q},\lambda\right)=\mathbf{0} \tag{37}$$

The virtual external work is given by

$$\begin{aligned}\delta\mathbf{q}^{\mathrm{T}}\mathbf{F}_{\text{ext}} &= -\int_{\Sigma}\delta\mathbf{u}^{\mathrm{h}}\cdot p(z,\lambda)\,\mathbf{n}\,ds \\ &= \int_{\Sigma}\delta\mathbf{u}^{\mathrm{h}}\cdot\rho g z^{\mathrm{h}}\mathbf{n}\,ds-\lambda\int_{\Sigma}\delta\mathbf{u}^{\mathrm{h}}\cdot h\,\mathbf{n}\,ds \qquad (38)\\ &= \delta\mathbf{q}^{\mathrm{T}}\mathbf{F}_{1}\left(\mathbf{q}\right)+\delta\mathbf{q}^{\mathrm{T}}\lambda\,\mathbf{F}_{2}\left(\mathbf{q}\right) \qquad (39)\end{aligned}$$

To solve the nonlinear problem with instabilities, we may use a constraint, known as the arc-length, that takes into account the control parameter λ as an additional unknown. The arc length, noted dl, depends on the displacement $\mathbf{q}_P$ of a set of points P and the fluid level parameter λ. Its expression is given by

$$dl=\sqrt{d\mathbf{q}_P^T d\mathbf{q}_P+\psi^2 d\lambda^2 h^2} \tag{40}$$

where ψ is a scale parameter such that $d\mathbf{q}_P^T d\mathbf{q}_P$ and $\psi^2 d\lambda^2$ have the same order of magnitude. A large value of ψ leads to a classical load control problem. On the contrary, if the ψ value is small, we are in the framework of a displacement control problem.

4.4. Remark on the numerical integration

A numerical issue comes from the fact that some finite elements are partially wetted for a given fluid height, inducing specific numerical integration of $\mathbf{F}_{\text{ext}}$,

$\mathbf{K}_{\text{fol}}$ or V_{f}. The numerical integrations of those operators have to be addressed. This is the purpose of Section 5 which presents an original level-set approach on quadratic meshes.

5. A level-set approach for numerical integration

5.1. Partially wetted elements

The tangent stiffness matrix and the nodal external forces are computed by numerical integration. However, because of the fluid volume conservation (incompressibility) and the slip condition of the fluid at the fluid-structure interface (inviscidity), some elements at the interface are partially wetted as seen in Fig. 5. Thereby, the initial discretization is no more appropriate at each Newton-Raphson iteration.

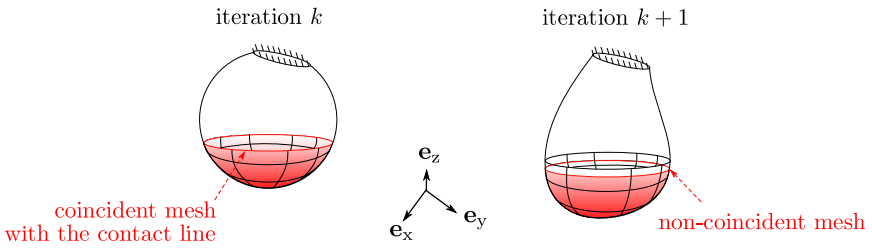

Figure 5: Surface elements partially wetted by the fluid with no coincident mesh between the wetted surface and the structural mesh after one Newton-Raphson iteration.

A simple classical approach consists in (i) finding the Gauss points on the wetted surface and the others ones on the dry surface and (ii) fixing the Gauss weight value to zero for all Gauss points on the dry surface. But we don't know the lack of accuracy due to the partially wetted elements integration of this approach. We propose in the following an other method to handle this integration by a level-set approach [4].

5.2. Level-set definition

By hypothesis, we neglect the effect of the surface tension. Thus, the level-set function can be defined by the equation of a plane of normal $\mathbf{e}_z$ at the height h such that

$$\phi(\mathbf{x}) = z - h \tag{41}$$

In this case, the internal face of the tank is separated by a line between a dry surface $\phi(\mathbf{x} > 0)$ and a wetted surface $\phi(\mathbf{x} < 0)$ as seen in Fig. 6.

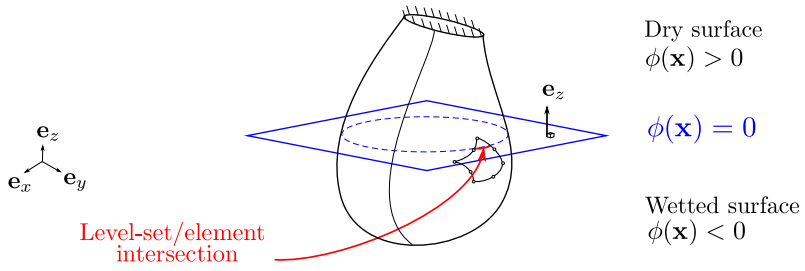

Figure 6: Definition of the level-set scalar function as a plane and its intersections with the internal face geometry (blue dashed line) and a surface finite element (in red line).

Finding the intersection line between the structural geometry and the plane could be difficult. In practice a finite element approximation of the level-set is done, so that we have to find the line equation expressed as

$$\phi^h(\mathbf{x}) = \sum_{i=1}^{N} \phi_i N_i = 0 \tag{42}$$

where N is the number of nodes. By splitting a partially wetted element, the integration based on a Gaussian quadrature is performed by evaluating new positions and weights of Gauss points, as see in Fig. 7.

This method is particularly useful for numerical integration computation of operators which depend on the free surface height. In our case, it concerns the external nodal forces vector $\mathbf{F}_{\text{ext}}$,the follower tangent stiffness matrix $\mathbf{K}_{\text{fol}}$ the fluid volume V_{f} of the free-surface area A_{f}.

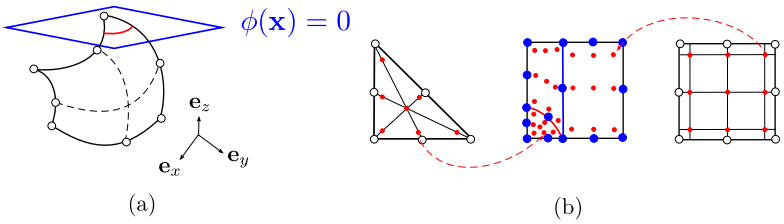

Figure 7: (a) Example of an element cutted by the level-set in the current configuration ; (b) New Gauss points postions in the isoparametric space.

5.3. Difficulties to split the quadratic elements

Approaches based on the computation of new positions and weights of Gauss points have been proposed for three nodes triangle elements in [11] and four nodes quadrilateral elements in [15]. In this paper, a major difficulty is due to the use of a quadratic surface element with height nodes. The main issue concerns the high number of possible intersections between a quadratical element and a plane. As seen in Fig. 8, an element could be cutted by two or more parts depending on the current configuration. Significant efforts have been made up to render the splitting-step algorithm flexible by taking into account all cases.

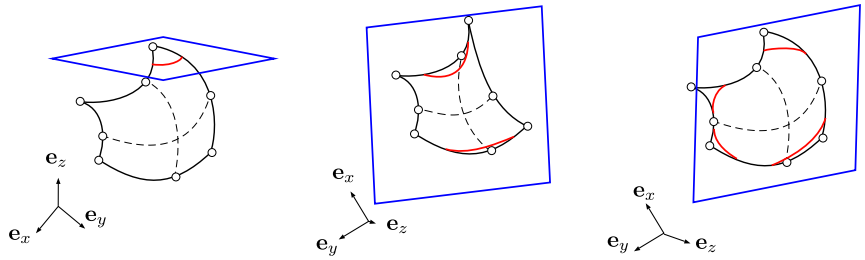

Figure 8: Non exhaustive set of intersections of the free-surface plane with a quadratic surface element in its current configuration. Over 255 cases could be encountered in theory.

5.4. Splitting method for a partially wetted element

To split one of the partilly wetted elements, i.e. to compute the curve of the contact line, our approach is the following:

(i) First, we evaluate the number of intersection points on the four boundaries of the reference surface element by computing the roots values of four quadratic equations:

$$\sum_{i=1}^{8} \phi_i N_i(1,\eta) = 0 \qquad \text{with} \quad \eta \in [-1,1] \tag{43}$$

$$\sum_{i=1}^{8} \phi_i N_i(-1,\eta) = 0 \qquad \text{with} \quad \eta \in [-1,1] \tag{44}$$

$$\sum_{i=1}^{8} \phi_i N_i(\xi,1) = 0 \qquad \text{with} \quad \xi \in [-1,1] \tag{45}$$

$$\sum_{i=1}^{8} \phi_i N_i(\xi,-1) = 0 \qquad \text{with} \quad \xi \in [-1,1] \tag{46}$$

(ii) Then, if there are only two intersection points, a large number of cases can be deduced from those illustrated in Fig. 9. Note that an internal point have to be computed to describe the curve inside the element. Also, wisely chosen rotations on the isoparametric subspace can be performed to minimize the number of implemented cases.

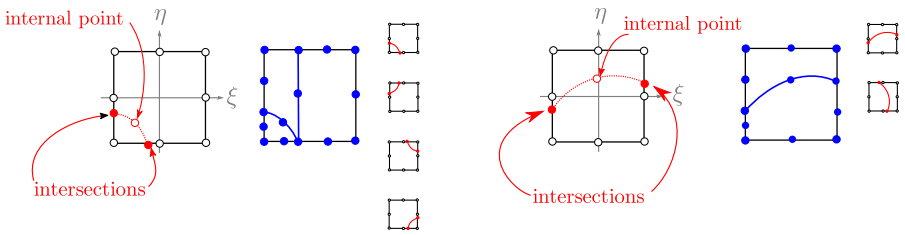

(a) (b)

Figure 9: The two cases of cutted elements widely encountered in practice (a) the intersection points are in two adjacent boundaries; (b) the intersection points are in two opposit boundaries. Note that various alternatives are possible to split the elements.

(iii) When there are more than two intersection points, without extra informations, the curve of the contact line is not unique (as seen in Fig. 10). To overcome this problem, we proceed to a regular splitting of the element until the sub-elements have only two intersection points (see Fig. 11).

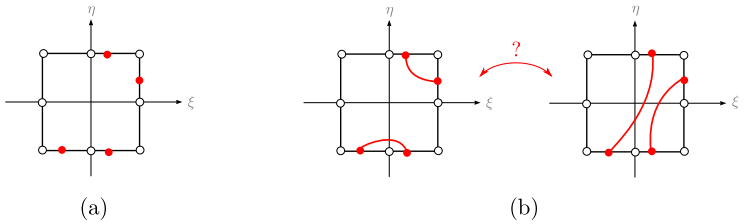

Figure 10: (a) Example of a case with four intersection nodes; (b) Two possibilities of cutted elements without extra informations than the number of intersection points.

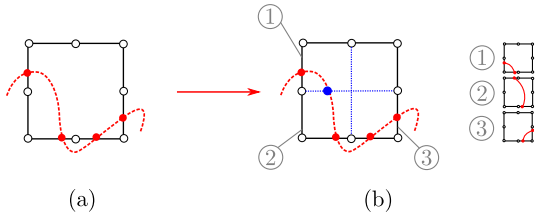

Figure 11: (a) Example of an element with four intersection points; (b) Regular spliting of the elements until all of the sub-elements have two intersection points.

Note that some particular cases cannot be treated with the previous method, as those illustrated in Fig. 12). So they have to be implemented one by one. Nevertheless, they are extremely rare when the structure is deformed. Indeed, they are generally encountered at the first step when we use structured meshes.

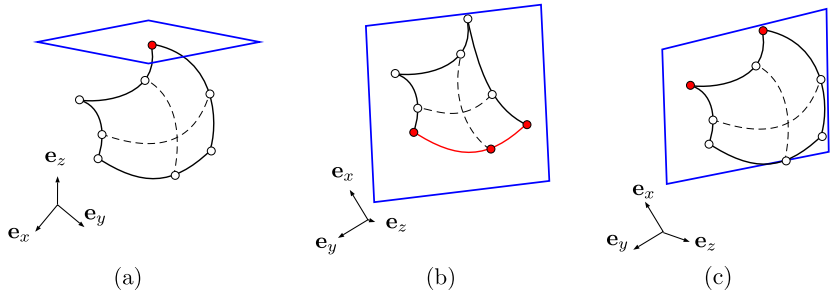

Figure 12: Non exhaustive set of specific cases that can't be treated with the splitting methodology, i.e. when (a) the intersection is a nodes; (b) the intersection is a boundary; (c) the intersection is two nodes.

Another issue concerns the size and the quality of the sub-elements. Since

the method is only used for integration, the size of the element does not influence the matrix conditioning nor the quality of the finite element solution. However, if the method is extended to an XFEM procedure [27], the sub-elements quality have to be taken into account.

5.5. Level-set example

In the following, we compute the free-surface area A_f, the wetted surface area A_Σ, and the fluid volume V_f of a filled hollow hexaedron illustrated in Figure 13 in function of the fluid height using a level-set approach. Only the surface mesh of the hexaedron is used in the simulation. This surface is defined by six quadratic 8-nodes quadrilateral elements. The goal is to compare (i) a classical integration method and (ii) the level-set approach described previously.

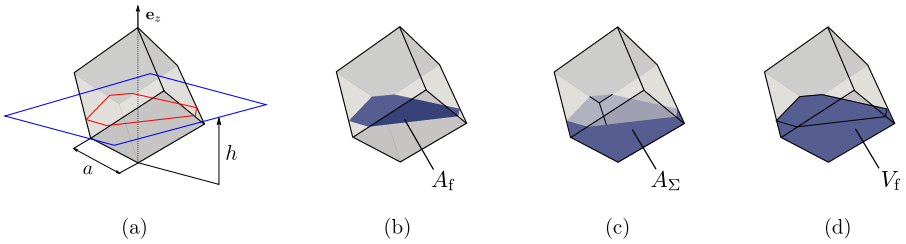

Figure 13: (a) Filling of rotated hexaedron with $a = 2$ m and visualization of (b) the free surface area A_f, (c) the wetted surface area A_Σ and (d) the fluid volume computation V_f.

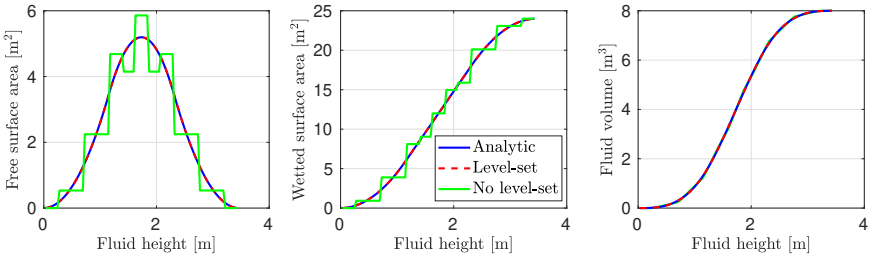

Figure 14: Evolution of the quantities which depend on the fluid height h: (a) the free surface area; (b) the wetted surface area; (c) the fluid volume above the free surface; For each quantities, the analytical solutions (blue line), the numerical computations with level-set (red dash line) or without level-set and $n_\mathrm{GP} = 9$ (green line) are given.

We can see the evolution of A_{f}, A_{Σ} and V_{f} in function of the fluid height in Figure 14. The level-set method shows very good agreements with the analytical solution for the three quantities. Then, the classical approach shows discontinuities on the free-surface area and the wetted surface but also very good agreements with the fluid volume computation as the three curves are superposed. Obviously, a fine mesh could minimize the error for the classical approach.

5.6. Conclusions about the level-set approach

We have proposed in Section 5 an original level-set approach to handle the numerical integration of the nodal external forces $\mathbf{F}_{\mathrm{ext}}$ and the follower forces tangent stiffness matrix $\mathbf{K}_{\mathrm{fol}}$. Indeed, the integration of those operators are done on partially wetted surface elements which depend on a varying free-surface height. The complexity of the method relies on the numerical implementation due to the large number of cases. Once this difficulty overcame, it is flexible and adapted to any curved surfaces meshed with quadratic elements with eight nodes. This development is the second major contribution to the paper. In Section 6, we propose three numerical examples showing the use of the level-set approach on complex geometries to compute the nonlinear equilibrium of structures submitted to hydrostatic follower forces.

6. Numerical examples

A 3D finite element code with the level-set approach has been developed to solve the nonlinear hydrostatic problem. In this section, three numerical examples are presented and analyzed: (i) the traction-torsion of a box with an initial fluid volume [7] and [10], (ii) the stretching and filling of a cylinder subjected to instabilities [13] and (iii) the filling and rotation of a hemispherical tank covered by a membrane. The objectives of those three examples are the validation of our algorithm by comparison to existing results from the literature

to show the effectiveness of the tangent stiffness operators in the convergence rate of our non-linear algorithms.

6.1. Box under traction/torsion

The first example, based on [7], concerns a box with an initial fluid height as seen in Fig. 15. The box is subjected to traction and torsion by prescribing displacements at the top and the bottom. The fluid volume V_{f} has to be equal to an initial fluid volume V_{init} during the simulation.

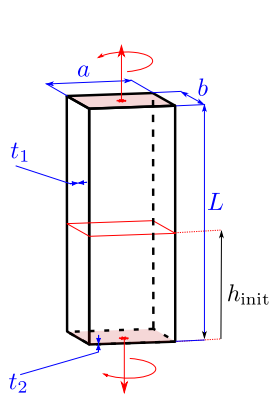

(a)

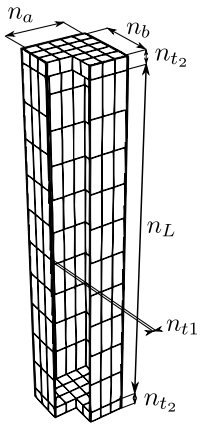

(b)

Geometry	Nb. elem.
$L = 0.3$ m	$n_L = 10$
$t_2 = 0.01$ m	$n_{t_2} = 1$
$t_1 = 0.001$ m	$n_{t_1} = 1$
$a = 0.05$ m	$n_a = 5$
$b = 0.05$ m	$n_b = 5$
$h_{\mathrm{init}} = 0.15$ m	

(c)

Figure 15: (a) Geometry parameters of the hollow box initially filled with water submitted to traction and torsion; (b) Sectional view of the mesh and its parameters; (c) Geomety and mesh parameters values.

No over-pressure is taken into account in the dry part of the box. A Saint-Venant Kirchhoff constitutive law is used with $E_1 = 0.75$ GPa for the structural body and $E_2 = 1$ GPa for the top and the bottom parts ($\nu = 0.3$ for both). This configuration avoid a snap-through behavior according to [7].

We plot in in Fig. 16 the evolution of the fluid height h, which satisfies the fluid volume constraint, in function of a load parameter $\lambda \in [0, 1]$. We obtain very good agreements between our results and those of [7]. We can see the deformed shape and the fluid free surface fluid in Fig. 17 at different time steps.

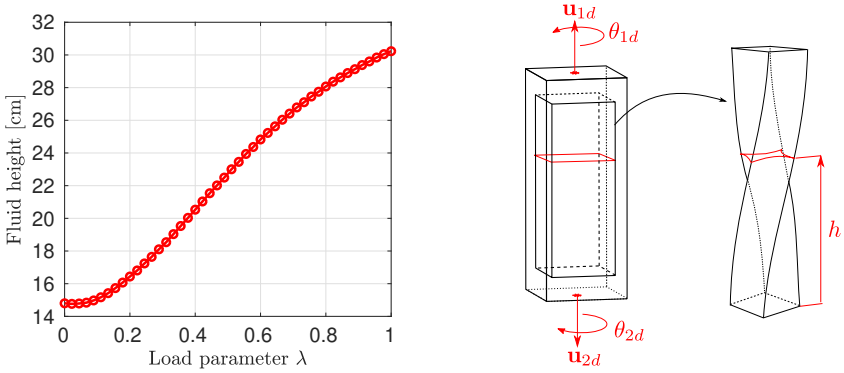

Figure 16: Response of the free surface height in term of a dimensionless parameter λ such that $\mathbf{u}_{1\mathrm{d}} = -\mathbf{u}_{2\mathrm{d}} = \lambda\, \mathrm{u}_{\max}\, \mathbf{e}_{\mathrm{z}}$ where $\mathrm{u}_{\max} = 0.0125$ m, and $\theta_{1\mathrm{d}} = -\theta_{2\mathrm{d}} = \lambda\pi/4$ rad .

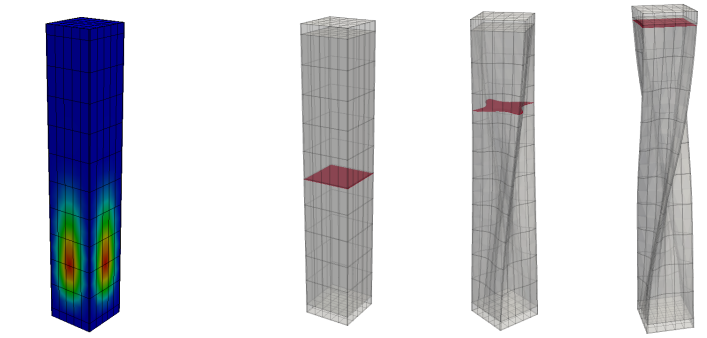

Figure 17: (a) Displacement magnitude of the structure between 0 (in blue) and 0.176 mm (in red) due to the hydrostatic pressure at $\lambda = 0$; (b) Deformed shape at $\lambda = 0$, $\lambda = 0.5$ and $\lambda = 1$. The free surface in red is represented just for the illustration because no free-surface mesh is needed for the computation.

Finally, the evolution of the out of balance norm $|| \mathbf{F}_{\mathrm{int}} - \mathbf{F}_{\mathrm{ext}} ||$ is shown in the Fig. 18 for various Newton-Raphson loops. A quadratic convergence rate is observed at each load step. To verify the fluid volume conservation, Fig. 18 show the fluid volume ratio at each bisection iteration when the fluid height is reevaluated during a Newton-Raphson loop ($\lambda = 0.5$ for example).

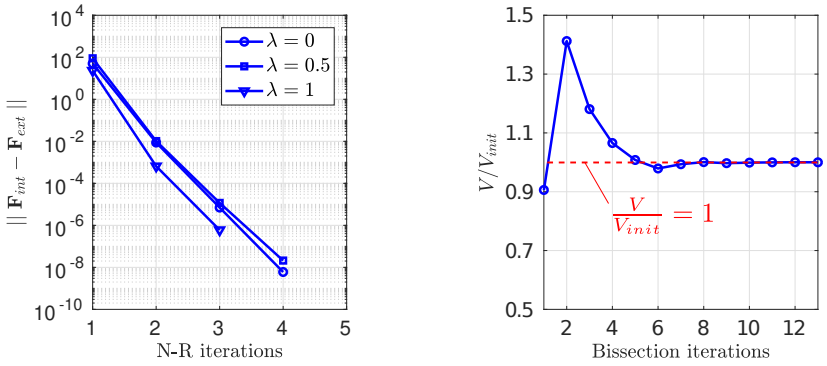

Figure 18: (a) Evolution of the out of balance norm at step 1 ($\lambda = 0.1$), step 5 ($\lambda = 0.5$) and step 10 ($\lambda = 1$); (b) Convergence of the bissection algorithm to ensure the fluid volume conservation at the first Newton-Raphson iteration for $\lambda = 0.5$.

6.2. Filling of a stretched cylinder

The second example, based on [13], concerns a cylinder stretched and filled with water (seen Fig. 19). Our objective is to evaluate the results of our code in comparison to [13]. The Mooney-Rivlin constitutive law (see Section 2) is chosen considering the following material parameters: $k = \frac{1}{7}$ and $\mu = 0.4225$ MPa with the relations $c_{10} + c_{01} = \frac{\mu}{2}$ and $k = \frac{c_{01}}{c_{10}}$. The bulk modulus k_0 is evaluated considering that $k_0 = \frac{E}{3(1-2\nu)}$ and $E = 6(c_{10} + c_{01})$ [20]. Note that E is the linearized Young modulus with no stretching and ν the Poisson ratio coefficient such that $\nu = 0.499$ to ensure the quasi-incompressibility of the structural material. A membrane element with no bending effect is used in [13]. In our case, quadratic hexaedron are choosen even if the structure is very thin : the ratio between the smallest side and the biggest side of an element may reach a maximum of 100 (whithout stretching). Moreover, because of large deformation, some elements may be distorded. Nevertheless, according to [28], the use of second order hexaerdral element minimize the effect of the mesh quality on the solution and our results are in good agreement with the reference solution.

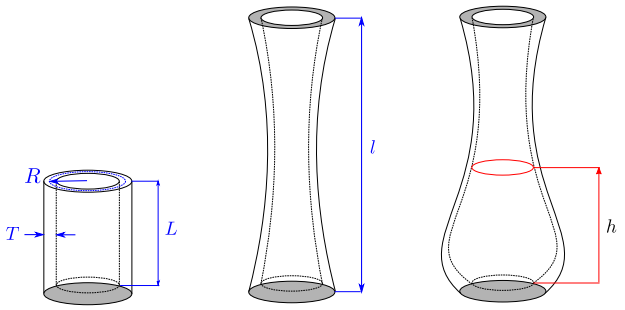

Geometry parameters
$R = 0.020$ m
$L = 0.160$ m
$l = 0.480$ m
$T = 8 \times 10^{-5}$ m

Figure 19: Stretching and filling of the rubber cylinder and its geometrical parameters.

In Fig. 20, we plot the evolution of the radial expansion in function of the fluid height. At first, considering only the stretching solution with no fluid, the converged radial expansion of three points (A, B and C) are in very good aggreement with [13]. As in the present example, the mesh quality does not affect our solution in this case. The filling process could be split in two parts: (i) a stable part where the fluid height increases during the filling process and (ii) an unstable part where the fluid height decrease as seen in Fig. 20. Fig. 21 shows the evolution of the fluid volume in function of the radial expansions of points A, B and C. These results are in very good agreements with those in [13].

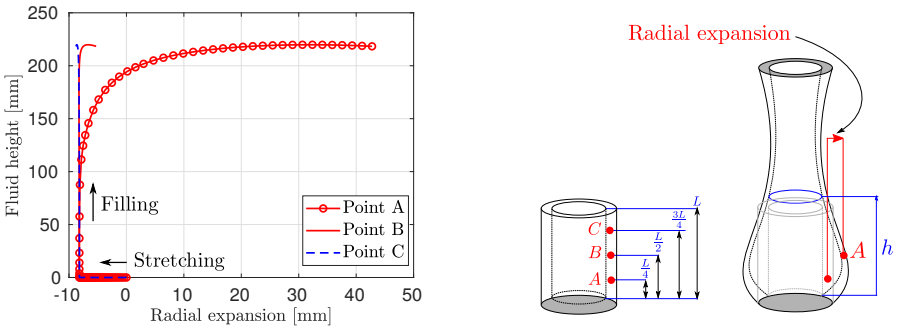

Figure 20: Evolution of the fluid height in function of the radial expansion of three points (A, B and C) after the stretching.

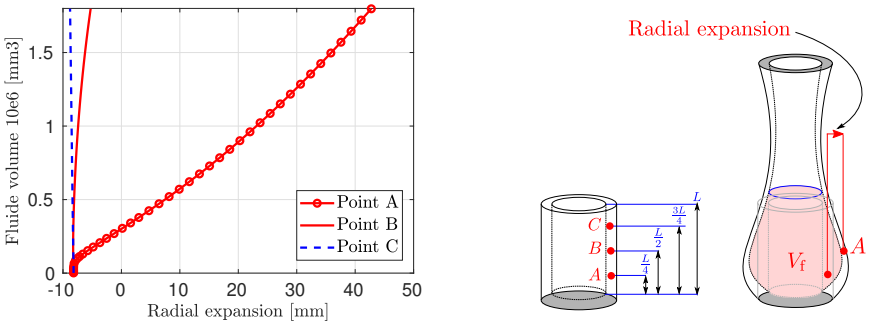

Figure 21: Evolution of the fluid volume in function of the radial expansion of three points (A, B and C) after the stretching.

In Fig. 22, we illustrate the current configuration of the structure at given fluid heights and the associated fluid volumes. We recall that the wetted surface does not depend on the structural fluid mesh since we use the level-set approach.

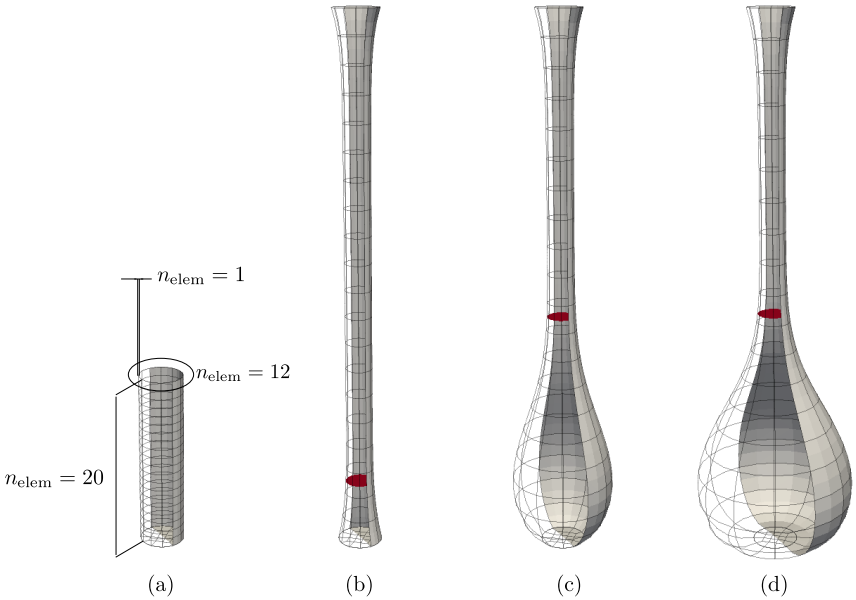

Figure 22: (a) Undeformed mesh of the structure; Current configurations at (b) $h_1 = 46.3$ mm and $V_1 = 0.02 \times 10^6$ mm^3; (c) $h_2 = 205.5$ mm and $V_2 = 0.401 \times 10^6$ mm^3; (d) $h_3 = 219.1$ mm and $V_3 = 260 \times 10^6$ mm^3. Note that the free surface in red is plotted only for illustration purpose.

The unstable solution is reached thanks to our continuation algorithm based on the arc-length method. The quadratic convergence rate of the iterative problem (see Fig. 23) is ensured by the tangent stiffness matrix. In fact, without the tangent stiffness matrix, our algorithm does not converge near unstable configurations. However, with the tangent stiffness matrix and the arc-length algorithm, a few Newton-Raphson iterations are needed to reach the nonlinear equilibrium state of the partially filled flexible tanks.

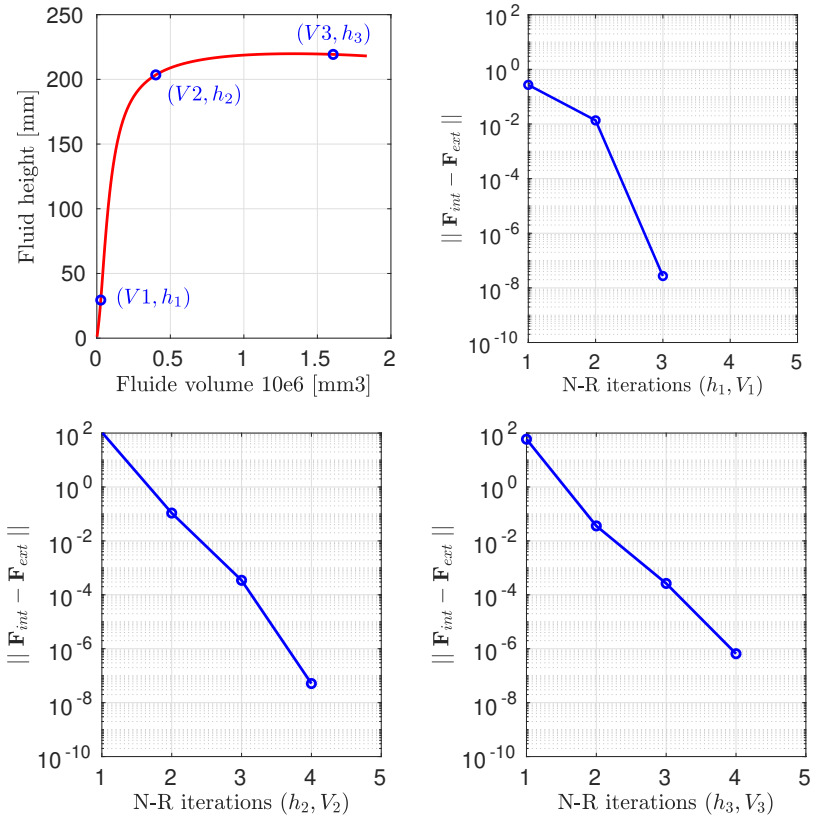

Figure 23: Evolution of the out of balance norm for three configurations illustrated in Fig. 22 with $h_1 = 46.3$ mm and $V_1 = 0.02 \times 10^6$ mm^3, $h_2 = 205.5$ mm and $V_2 = 0.401 \times 10^6$ mm^3, $h_3 = 219.1$ mm and $V_3 = 260 \times 10^6$ mm^3.

6.3. Filling and rotation of a hemispherical tank covered by a stretched membrane

We propose an original last example which consists in finding the nonlinear equilibrium of a stretched membrane covering a rigid hemispherical tank of radius r partially filled with fluid. The simulation is illustrated in Figure 24 and is separated in three phases:

- **Phase 1:** stretching of a membrane with an initial radius R_0 ;
- **Phase 2:** filling of the tank ;
- **Phase 3:** rotation of the rigid part of the tank for a given prescribed fluid volume.

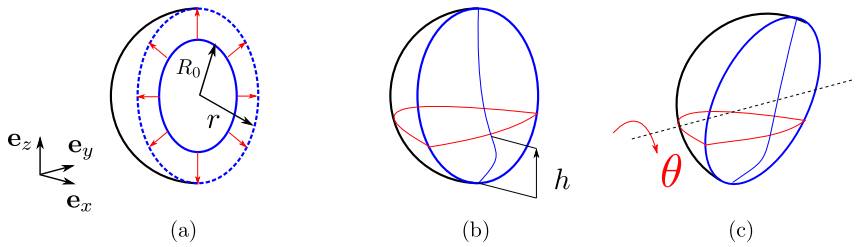

Figure 24: (a) **Phase 1:** Stretching of the membrane of initial radius R_0 which cover the rigid hemispherical tank of radius r; (b) **Phase 2:** Filling of the tank parameterized by the fluid height h form $h = 0$ to $h = h_{\max}$; (c) **Phase 3:** Rotation of the whole fluid-structure system constrained by an initial fluid volume conservation.

No dynamical effects are taken into account because the transformations are supposed to be quasi-static. The objectives of this example are to illustrate the two types of loading enable by our algorithms: (i) the fluid loading directly parameterized by the fluid height h and (ii) the fluid loading parameterized by a fluid height for a given fluid volume during a transformation with large displacement (i.e. a large rotation θ of the rigid tank).

Phase 1: The stretching

The initial geometrical parameters of the membrane are the initial radius $R_0 = 0.10$ m and the initial thickness $T = 0.4$ mm. The Mooney-Rivlin constitutive law is chosen considering the following material parameters: $k = \frac{1}{10}$ and $\mu = 0.4225$ MPa with the relations $c_{10} + c_{01} = \frac{\mu}{2}$ and $k = \frac{c_{01}}{c_{10}}$ (see sub-section 6.2). The mesh of the elastic membrane is a volumetric 20 nodes hexaedron mesh and only the internal surface of the rigid tank is meshed using 8 nodes quadrilateral elements. The rigid tank mesh is mandatory to compute the fluid volume V_{f}, the free-surface area A_{f} and all operators which depend on those two terms. The mesh parameters on the reference configuration of the elastic structure and the rigid tank are described in Figure 25.

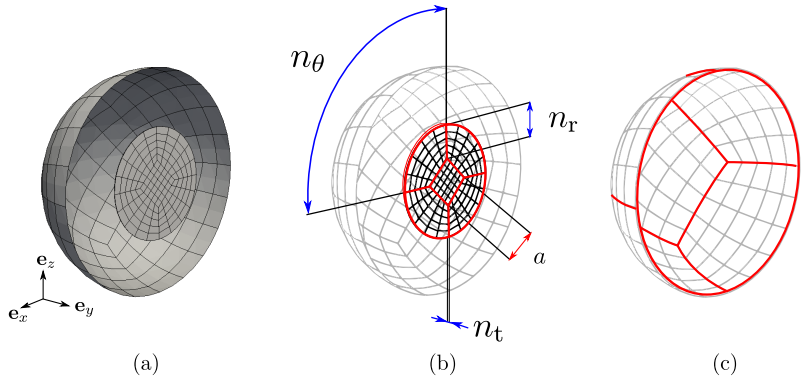

Figure 25: (a) Visualization of the membrane and the tank meshes; (b) mesh parametrization of the elastic structure with 20 nodes hexadron with the number of elements in the circumference quadrant n_θ, the thickness n_{t} and the radius part n_{r}, the number of elements in the thickness is fixed with $n_{\mathrm{t}} = 1$ and the value a is needed to construct the quadrilateral mesh with $a = 0.3R_i$; (c) Mesh of the rigid tank needed to compute the fluid volume and the free surface area.

In phase 1, we solve the nonlinear problem to find the displacement of the stretched membrane $\mathbf{u}_{\mathrm{str}}$ such that $\mathbf{x} = \mathbf{X} + \mathbf{u}_{\mathrm{str}}$, considering a prescribed displacement as seen in Figure 26.

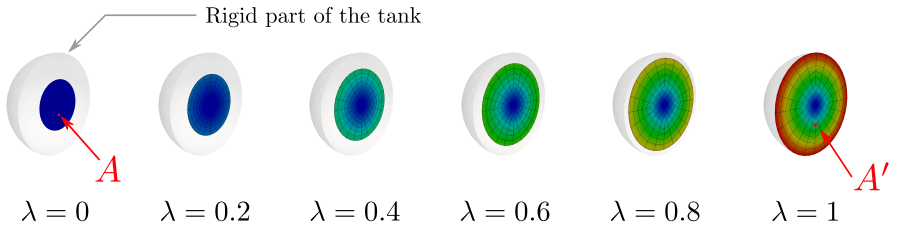

Figure 26: Solutions of a nonlinear problem with prescribed displacement from a reference membrane of radius $R_0 = 0.1$ m to a stretched membrane of radius $r = 0.2$ m. λ is a load parameter such that $\lambda = 0$ (no stretch) and $\lambda = 1$ (fully stretched). The points A' corresponds to the current position of a point A such that $\mathbf{X}_\mathrm{A} = (0, -0.3R_i, 0)$ in the reference configuration and $\mathbf{X}_\mathrm{A} + \mathbf{u}_\mathrm{str}(\mathbf{X}_\mathrm{A})$ in the current configuration.

Phase 2: The filling

In phase 2, we want to evaluate the displacement $\mathbf{u}_\mathrm{fil}$ when the tank is filled such that $\mathbf{x} = \mathbf{X} + \mathbf{u}_\mathrm{str} + \mathbf{u}_\mathrm{fil}(h)$. In the following, our quantity of interest (QOI) is the norm of the displacement $q = || \mathbf{u}_\mathrm{fil}(\mathbf{X}_\mathrm{A}) ||$ illustrated in Figure 30. In order to validate our mesh, we want to ensure that the QOI do not depend on the mesh discretization when the tank is fully filled. The Table 1 gives the values of q for various mesh parameters n_θ and n_r. As seen in Figure 27, the (QOI) for $n_\mathrm{dof} = 1188$ corresponding to $(n_\theta = 5, n_\mathrm{r} = 5)$ has less than 0.5 % of error compared to the reference solution q_ref. An illustration of the fully filled state for various mesh and the selected one are given in Figure 28.

(n_θ, n_r)	$(1,1)$	$(2,2)$	$(5,5)$	$(10,10)$	$(20,20)$	$(40,40)$
n_elem	5	20	125	500	1200	8000
n_dof	144	489	1188	4623	18243	169209
q (mm)	11.03	11.77	11.81	11.83	11.85	$q_\mathrm{ref} = 11.86$

Table 1: Number of elements and degrees of freedom (dof) with the mesh parametrization

On the selected mesh, we perform a filling simulation from $h = 0$ mm to $h = 180$ mm with a length step $dh = 20$ mm. Some snapshots are illustrated in

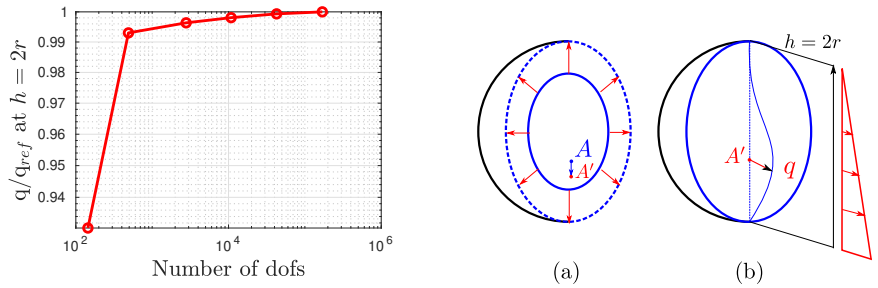

Figure 27: Converged displacement due to the fluid pressure q for various meshes divided by a reference q_{ref} for a very fine mesh ($n_\theta = 40, n_\mathrm{r} = 40$) at $h = 2r$ mm; (a) Prescribed displacement from step 1; (b) Fully filled tank with hydrostatic pressure and the (QOI).

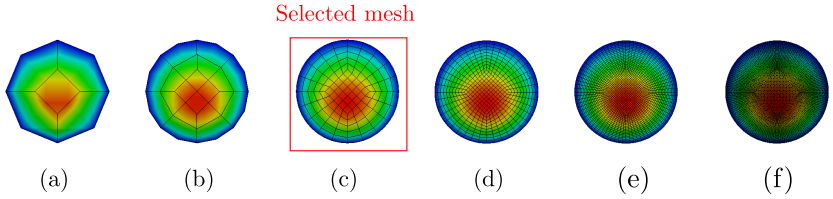

Figure 28: Displacement field $\mathbf{u}_{\mathrm{fil}}$ of the membrane when the tank is fully filled for various mesh parameters (n_θ,n_r): (a) $(1,1)$; (b) $(2,2)$; (c) $(5,5)$; (d) $(10,10)$; (e) $(20,20)$; (f) $(40,40)$.

Figure 29 where the wetted surface is not coincident with the mesh discretization due to the level-set approach. The evolution of q is given in Figure 30 and show a nonlinear response due to the fluid pressure parameterized by the fluid height.

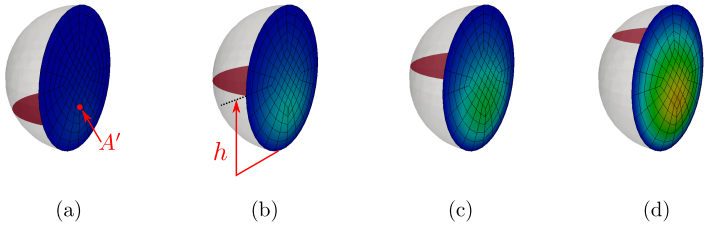

Figure 29: (a) Initial mesh befors streching; Displacement magnitude $\mathbf{u}_{\mathrm{fil}}$ of the membrane between 0 mm (in blue) and 10.6 mm (in red) due to the hydrostatic pressure for various prescribed fluid height:(a) $h = 50$ mm; (b) $h = 100$ mm; (c) $h = 120$ mm; (d) $h = 160$ mm. Note that the free surface in red is plotted only for illustration purpose.

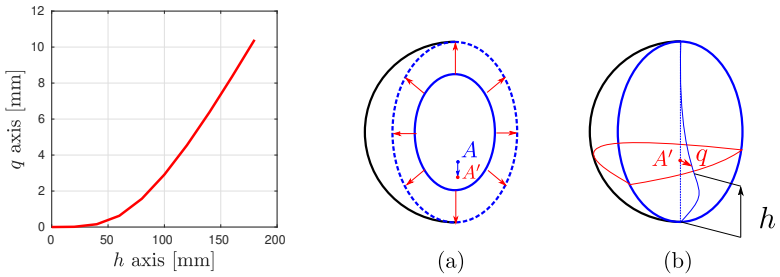

Figure 30: Evolution of q in function the fluid height; (a) Displacement of the point $A = (0, 0, -0.3R_i)$ to A' due to the stretching; (b) Displacement due to the fluid pressure minus the displacement due to the stretching at point A'.

In order to show the influence of $\mathbf{K}_{\text{fol}}$ on the convergence rate of the Newton-Raphson algorithm, we performed two simulations. One simulation is done with $\mathbf{K}_{\text{fol}}$ and the other one without. In Fig. 31, we can visualize the decrease of the out of balance error norm $\varepsilon = || \mathbf{F}_{\text{int}} - \mathbf{F}_{\text{ext}} ||$ in function of the number of Newton-Raphson iterations.

The curves in Fig. 31 shows an important contribution of the tangent stiffness matrix $\mathbf{K}_{\text{fol}}$ on the convergence rate. Indeed, the number of iterations needed to reach a given ε with $\mathbf{K}_{\text{fol}}$ (between 3 or 4 iterations) is lower than the ones need without $\mathbf{K}_{\text{fol}}$ (between 6 or 9). The stagnation is due to the numerical errors when no criterion is given. This example, in which the fluid height is the control parameter, is particularly relevant to show the contribution of the two key points developed in the paper: (i) the influence of the follower tangent stiffness matrix, and (ii) the use of an original level-set approach with a quadratic surface mesh.

Phase 2: The rotation

The last phase consists in prescribing a displacement, precisely a rotation around $(O, \mathbf{e}_{\text{x}})$, on the boundary of the membrane with a fluid volume conservation constrained ensured by a dichotomy algorithm at each Newton-Raphon

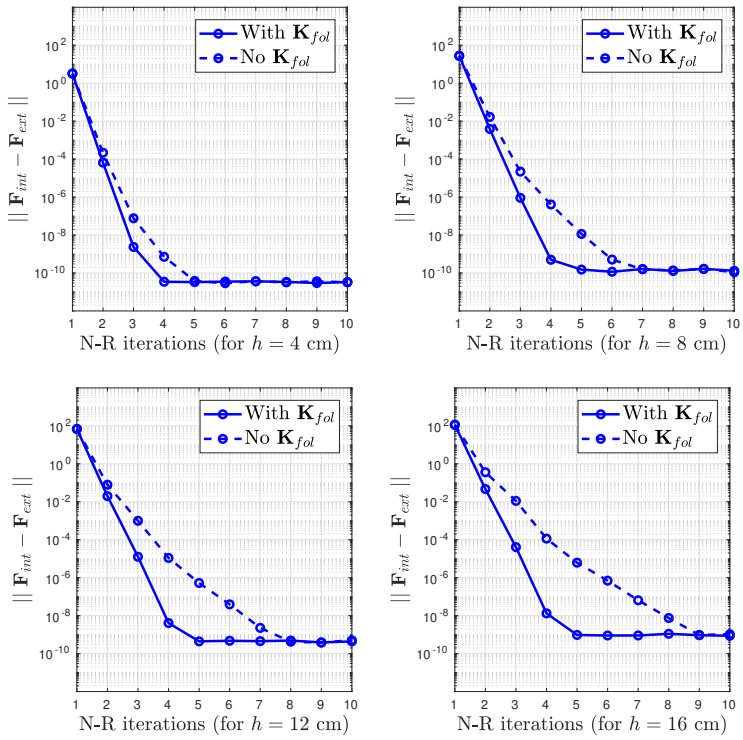

Figure 31: Influence of the follower forces tangent stiffness matrix on the Newton-Raphson algorithm convergence for various fluid heights (i.e. $h = 40$ mm, $h = 80$ mm, $h = 120$ mm and 160 mm).

iterations. The displacement associated is noted $\mathbf{u}_{\text{rot}}$ such that $\mathbf{x} = \mathbf{X} + \mathbf{u}_{\text{str}} + \mathbf{u}_{\text{rot}}(\text{V}_\text{f})$. In Figure 32 we plot two configurations of the deformed tank, one in the current configuration and the other on a reference coordinate system fixed at the rigid part. The prescribed angle is given from $\theta \in [0, 360]$ degrees with a step $d\theta = 1.8$ degrees. The initial fluid volume is such that $V_\text{f} = 1.0e^{-3}$ m^3.

As we can see in Figure 33, the fluid height is varying during the simulation to conserve the fluid volume. We also plot the (QOI) in function of the angle. Note that between $\theta = 230$ degrees to 270 degrees, the membrane is not subjected to a fluid pressure, so the (QOI) is null.

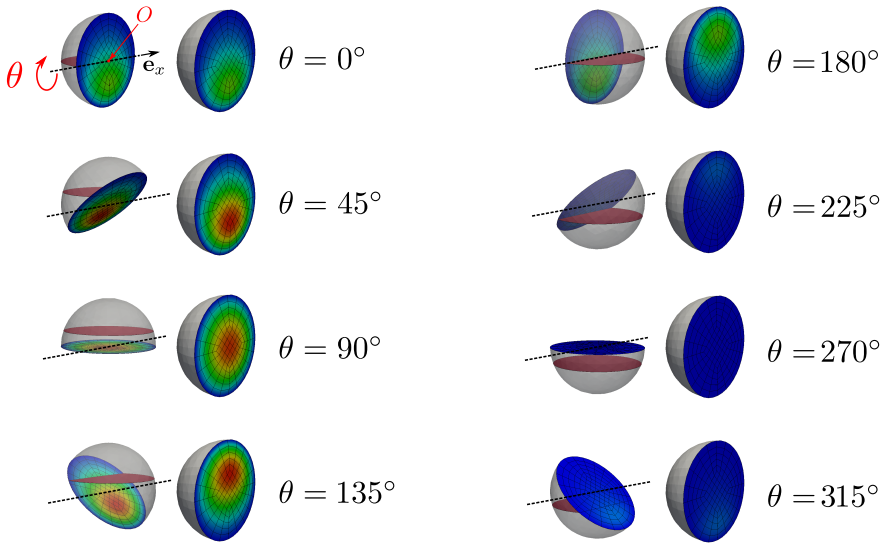

Figure 32: Snapshots of the magnitude of $||\ \mathbf{u}_{\text{rot}}\ ||$ due to the fluid pressure for various prescribed rotation θ around $(O, \mathbf{e}_x)$ and a given initial fluid volume $V_{\text{f}} = 1.0e^{-3}$ m^3 in the current configuration and a fixed reference coordinate system (in blue $||\ \mathbf{u}_{\text{rot}}\ ||= 0$ and in red $||\ \mathbf{u}_{\text{rot}}\ ||= 4.55$ mm). Note that the free surface in red is plotted only for illustration purpose.

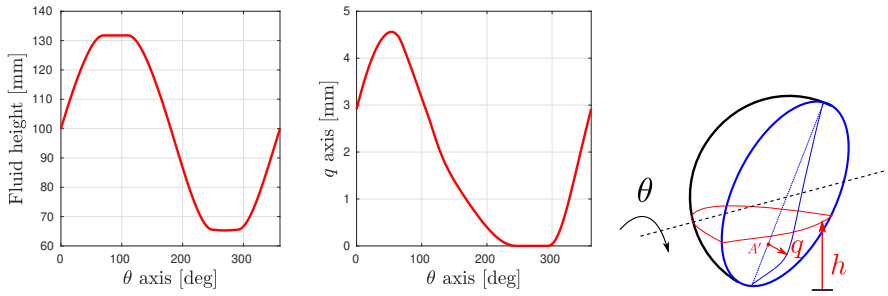

Figure 33: Evolution of the fluid height and the (QOI) in function of θ between $\theta = 0$ degrees to $\theta = 360$ degrees.

Finally, we plot the evolution of the out of balance vector for various θ angles and the convergence is still very efficient on Figure 34. A slight decrease of the

convergence is observed for the second Newton-Raphson iteration but not the others. Indeed a few Newton-Raphson iterations are needed (around 3 or 4) to reach a satisfying error with our approach.

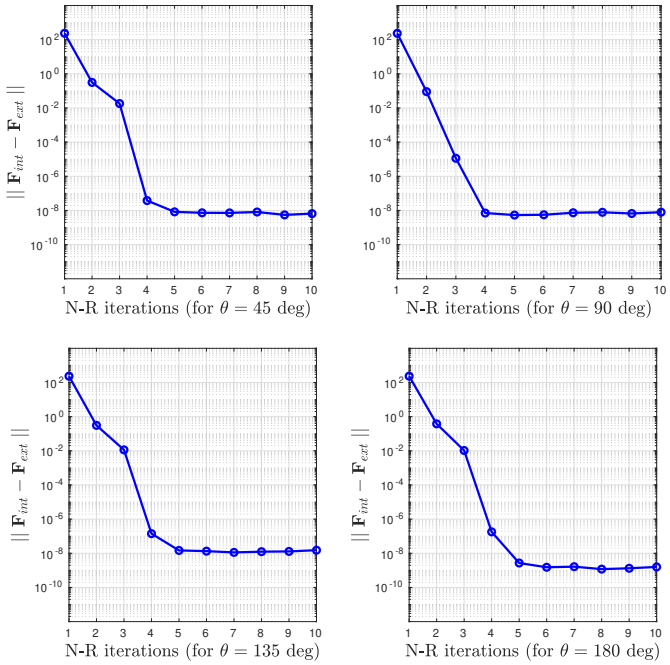

Figure 34: Evolution of out of balance vector during the Newton-Raphson loops for: (a) $\theta = 45$ degrees; (b) $\theta = 90$ degrees; (c) $\theta = 135$ degrees; (d) $\theta = 180$ degrees.

6.4. Conclusion and remarks on the numerical examples

The three numerical examples detailed previously concern the nonlinear equilibrium of 3D elastic structures submitted to hydrostatic follower forces by using a level-set method for the numerical integration. The first example illustrates the use of our method when a structure containing a initial amount of fluid volume is submitted to prescribed displacements. The fluid height is reevaluated by bisection to conserve the fluid volume. Our results are in very good agreements with literature [7]. The second one concerns a problem solved by an arc-length method to pass through instability of a very flexible structure. The results are

here also in good agreement with the reference literature [11]. Then the last original example shows the beneficial influence of the follower forces tangent stiffness matrix to reach a quadratic convergence rate of the Newton-Raphson algorithm when the fluid height is the controlled parameter. This example also shows the flexibility of the level-set approach when the fluid volume is prescribed. In a nutshell, those examples have been implemented to illustrate and validate our two main contributions of the paper which are:

- the influence of the tangent stiffness matrix, in particular the follower force contribution, to solve a nonlinear problem of structures submitted by hydrostatic forces;
- the use of an original level-set approach to compute the numerical integration of the external force $\mathbf{F}_{\text{ext}}$ and the follower forces tangent stiffness matrix $\mathbf{K}_{\text{fol}}$ on the quadratic partially wetted surface elements.

7. General conclusion and outlooks

In this paper, the nonlinear equilibrium of flexible tanks partially filled with liquid submitted to hydrostatic follower forces has been investigated. A Newton-Raphson algorithm, based on the finite element method in 3D combined with an original level-set approach, has been implemented. The nonlinear formulation with prescribed displacement has also been recalled for stable and unstable systems. The main contributions of this work are the use of a level-set approach to perform the numerical integration of partially wetted quadratic surface elements. This last aspect is used to compute accurately the external force $\mathbf{F}_{\text{ext}}$ and the follower tangent stiffness matrix $\mathbf{K}_{\text{fol}}$ when the wetted surface is not coincident with the structural mesh. This contribution have been used for the resolution of numerical examples by using a volumetric hexaedron quadratic mesh. The obtained results are in very good agreement with the literature [7, 13] and validate our algorithm. Then, an original example showing the significant contribution of the follower forces is presented, either if the fluid height is the controlled pa-

rameter or for prescribed displacement with a given fluid volume. In extension to this work, the prestressed state due to geometrical nonlinearities can be used for the dynamic computation of elastic tanks containing an internal free-surface liquid around its current configuration. The proposed level-set developments could also be an interesting way to explore the computation of the nonlinear elastic deformations of structures filled with a liquid, considering surface tensions effects, which is still an open problem (actual softwares as Evolver [29] only compute the liquid free-surface equilibrium in rigid tanks).

Acknowledgments

This work was funded by the French Ministry of National Education, Higher Education and Research through a three year scholarship for doctoral studies related to fluid-structure interaction.

References

[1] H. J.-P. Morand, R. Ohayon, Fluid Structure Interaction, John Wiley & Sons, 1995.

[2] M. Chiba, Nonlinear hydroelastic vibration of a cylindrical tank with an elastic bottom, containing liquid. part i: Experiment, Journal of Fluids and Structures 6 (1992) 181–206. doi:10.1016/0889-9746(92)90044-4.

[3] J.-S. Schotté, S. Carra, M. Amabili, R. Ohayon, Nonlinear effect of hydrostatic pressure on the hydroelastic vibrations of a plate, in: Proceedings of the Second International Conference on Dynamics, Vibration and Control, CUSTOM, Beijing, China, 2006.

[4] J. A. Sethian, A fast marching level set method for monotonically advancing fronts, Proceedings of the National Academy of Sciences 93 (1996) 1591–1595.

[5] H. D. Hibbitt, Some follower forces and load stiffness, International Journal for Numerical Methods in Engineering 14 (1979) 937–941. doi:10.1002/nme.1620140613.

[6] T. Rumpel, K. Schweizerhof, M. Haßler, Volume-dependent pressure loading and its influence on the stability of structures, International Journal for Numerical Methods in Engineering 56 (2) (2003) 211–238. doi:10.1002/nme.561.

[7] T. Rumpel, K. Schweizerhof, Hydrostatic fluid loading in non-linear finite element analysis, International Journal for Numerical Methods in Engineering 59 (6) (2004) 849–870. doi:10.1002/nme.892.

[8] T. Rumpel, K. Schweizerhof, Efficient finite element modelling and simulation of gas and fluid supported membrane and shell structures, Textile Composites and Inflatable Structures, Springer, Dordrecht 3 (2005) 153–172. doi:10.1007/1-4020-3317-6_10.

[9] M. Haßler, K. Schweizerhof, On the influence of fluid-structure-interaction on the stability of thin-walled shell structures, International Journal of Structural Stability and Dynamics 07 (2007) 313–335. doi:10.1142/S0219455407002277.

[10] M. Haßler, K. Schweizerhof, On the static interaction of fluid and gas loaded multi-chamber systems in large deformation finite element analysis, Computer Methods in Applied Mechanics and Engineering 197 (19–20) (2008) 1725–1749. doi:10.1016/j.cma.2007.08.028.

[11] Y. Zhou, A. Nordmark, A. Eriksson, Instability of thin circular membranes subjected to hydro-static loads, International Journal of Non-Linear Mechanics 76 (2015) 144–153. doi:10.1016/j.ijnonlinmec.2015.06.010.

[12] A. Patil, A. Nordmark, A. Eriksson, Wrinkling of cylindrical membranes with non-uniform thickness, European Journal of Mechanics - A/Solids 54 (2015) 1–10. doi:10.1016/j.euromechsol.2015.05.015.

[13] A. Eriksson, A. Nordmark, A. Patil, Y. Zhou, Parametric stability investigations for hydro-statically loaded membranes, Computers and Structures 174 (2016) 33–41. doi:10.1016/j.compstruc.2015.08.014.

[14] Y. Zhou, A. Nordmark, A. Eriksson, Multi-parametric stability investigation for thin spherical membranes filled with gas and fluid, International Journal of Non-Linear Mechanics 82 (2016) 37–48. doi:10.1016/j.ijnonlinmec.2016.02.005.

[15] K.-H. Lee, P.-S. Lee, Nonlinear hydrostatic analysis of flexible floating structures, Applied Ocean Research 59 (2016) 165–182. doi:10.1016/j.apor.2016.05.016.

[16] M. Amabili, Nonlinear Mechanics of Shells and Plates: Composite, Soft and Biological Materials, Cambridge University Press, New York, USA, 2018.

[17] G. A. Holzapfel, Nonlinear solid mechanics, John Wiley & Sons, 2001.

[18] J. C. Simo, R. L. Taylor, Quasi incompressible finite elasticity in principal stretches, Computer Methods in Applied Mechanics and Engineering 85 (1991) 273–310. doi:10.1016/0045-7825(91)90100-K.

[19] P. Steinmann, M. Hossain, G. Possart, Hyperelastic models for rubber-like materials: consistent tangent operators and suitability for treloars data, Archive of Applied Mechanics 82 (2012) 1183–1217. doi:10.1007/s00419-012-0610-z.

[20] N.-H. Kim, Introduction to Nonlinear Finite Element Analysis, Springer, 2015.

[21] M. A. Crisfield, Non-linear finite element analysis of solids and structures, Vol. 1, John Wiley & Sons, 1994.

[22] T. Belytschko, W. K. Liu, B. Moran, K. Elkhodary, Nonlinear finite elements for continua and structures, 2nd Edition, John Wiley & Sons, 2014.

[23] M. Amabili, I. D. Breslavsky, Displacement dependent pressure load for finite deflection of doubly-curved thick shells and plates, International Journal of Non-Linear Mechanics 77 (2015) 265 – 273. doi:10.1016/j.ijnonlinmec.2015.09.007.

[24] O. C. Zienkiewicz, R. L. Taylor, Non-linear finite element analysis of solids and structures, Vol. 2, Butterworth-heinemann, 2000.

[25] C. Hoareau, J.-F. Deü, Non-linear finite element analysis of an elastic structure loaded by hydrostatic follower forces, Procedia Engineering 199 (2017) 1302–1307. doi:doi.org/10.1016/j.proeng.2017.09.320.

[26] J.-S. Schotté, R. Ohayon, Incompressible hydroelastic vibrations: finite element modelling of the elastogravity operator, Computers and Structures 83 (2–3) (2005) 209–219. doi:10.1016/j.compstruc.2004.03.084.

[27] N. Moës, J. Dolbow, T. Belytschko, A finite element method for crack growth without remeshing, International Journal for Numerical Methods in Engineering 46 (1999) 131–150. doi:10.1002/(SICI)1097-0207(19990910)46:1<131::AID-NME726>3.0.CO;2-J.

[28] E. T. Ooi, S. Rajendran, J. H. Yeo, A 20-node hexahedron element with enhanced distortion tolerance, International Journal for Numerical Methods in Engineering 60 (2004) 2501–2530. doi:10.1002/nme.1056.

[29] K. A. Brakke, The surface evolver, Experimental Mathematics 1 (1992) 141–165 . doi:10.1080/10586458.1992.10504253.